applied sciences

MDPI

Article

On the Characteristics of EMTR as a Correlation-Estimator-Based Fault Location Method in Transmission Lines

Akif Nadeem [1], Yanzhao Xie [1,*], Shaoyin He [1], Ning Dong [1], Pietro Caccavella [1] and Maria Saleem [2]

[1] State Key Laboratory of Electrical Insulation and Power Equipment, School of Electrical Engineering, Xi'an Jiaotong University, Xi'an 710049, China
[2] School of Energy and Power Engineering, Xi'an Jiaotong University, Xi'an 710049, China
* Correspondence: yzxie@xjtu.edu.cn

Abstract: Methods based on electromagnetic time reversal (EMTR) have recently demonstrated promising results. In particular, EMTR, as a correlation estimator metric, has offered a quantitative definition for fault location candidates. As the correlation estimator already obtains the system transfer functions by simulating fault occurrences, these functions are subsequently correlated with the fault-generated transfer function. Therefore, it is necessary to explore the analysis related to the pre-fault processing of this metric. Firstly, the impact of fault impedance mismatch between the fault occurrence and fault estimation stages was investigated, and a simple approach is presented after observing the fault locations' error. Secondly, it was noticed that the existing correlation estimator approach does not accurately identify fault types; therefore, a pseudo approach was developed to address this issue. Finally, the spatial step considered during the fault estimation stage was investigated. It is demonstrated that larger spatial steps result in inaccuracies in fault location. The smaller spatial steps improved the performance, but increased the memory burden on the data storage devices, especially when simple and pseudo approaches must be employed. The memory issue was resolved by presenting a hybrid approach that makes use of regression analysis. A single-phase and a three-phase lossy transmission line system were used to illustrate the proposed analyses.

Keywords: transmission lines; fault location; correlation estimator method; regression analysis

Citation: Nadeem, A.; Xie, Y.; He, S.; Dong, N.; Caccavella, P.; Saleem, M. On the Characteristics of EMTR as a Correlation-Estimator-Based Fault Location Method in Transmission Lines. *Appl. Sci.* **2023**, *13*, 280. https://doi.org/10.3390/app13010280

Academic Editor: Gaetano Zizzo

Received: 25 November 2022
Revised: 19 December 2022
Accepted: 20 December 2022
Published: 26 December 2022

1. Introduction

Faults on transmission lines disrupt the smooth operation of power systems; the robust finding of their location plays a vital role. Various fault location methods have been developed over the years; two categories, namely impedance-based methods [1,2] and travelling-wave-based methods [3,4], are well known. In the impedance-based methods, the fault position is determined by analysing the voltage and current measurements taken before and after the fault event, while in travelling-wave-based methods, the fault locations are computed by exploiting the transient signals produced by the fault. The accuracy of impedance-based methods can be influenced by the line configuration, fault resistance, load imbalance, and the presence of distributed generation sources [5–7]. On the other hand, the disadvantages of travelling-wave-based methods are as follows: (a) The data acquisition requires complicated signal processing techniques. (b) The problem of synchronising the time between multiple observation points is challenging. (c) In lossy transmission lines, the travelling waves will be distorted and attenuated during signal propagation. Therefore, the accurate calculation of the arrival time will be challenging. (d) In scenarios involving branched lines, fault-generated transient signals have to propagate over numerous junctions and will experience attenuation, resulting in a decrease in their intensity. (e) In a mixed overhead–undergroundcable transmission line power system, the travelling speed difference between multiple media will cause location bias [7–10].

The time reversal theory, which was initially applied to the acoustic field, is used to address the issues of travelling-wave-based methods, in which ultrasonic pressure fields are recorded, time-reversed, re-emitted, and focused on the source target [11]. Recent applications of time reversal theory to electromagnetics have led to the development of a method called the EMTR-based disturbance localisation method. It has been utilised for the localisation of flash-overs and lightning discharges, where it has been demonstrated that the wave fronts generated by time-reversed electromagnetic fields are focused at lightning strike locations [12]. This concept is then employed for fault location in power grids, in which fault-generated transients observed at specific observation points are time-reversed and sent back to the same simulated system, focusing on the fault position [5,7]. In this regard, researchers have extended its application to various power system network topologies while proposing new metrics and design criteria for fault position estimation. Razzaghi et al., for example, investigated the use of EMTR-based fault location algorithms in systems such as series-compensated, overhead–underground mixed cable, and multi-terminal HVDC transmission line networks [13,14]. In [15], an alternative approach to that of [7] was proposed, where the fault position was determined on the basis of a particular range of the arguments of the voltage and transfer function. The authors of [16] showed that the computed fault signals at the actual fault position were the time-delayed copies of the fault-generated transient signals. The concept of mirrored minimum energy was proposed in [17], where it was demonstrated that, when time-reversed signals are back-propagated, their energy is minimum at the actual fault position. In [18], the EMTR-based norm criteria, namely the two-norm and P-norm for fault location computation, were introduced, and it was confirmed that the P-norm performed better. Moreover, The EMTR technique has been validated experimentally on a full-scale setup [19].

Currently, the EMTR technique can be defined as a correlation estimator between the transfer functions of the fault occurrence and fault estimation stages, yielding the correlation coefficient value (CCv) at the corresponding guessed fault location (GFL) [8]. The correlation estimator metric is time-efficient compared to other EMTR metrics, because, in other metrics, the time-reversed transients are injected back into the same system and a large number of simulation batches are performed after the fault's occurrence, whereas, for the correlation estimator metric, the database in the form of the transfer functions of the same system is already available to correlate with the fault-generated transfer function. Furthermore, its quantitative property outperforms other EMTR metrics in terms of offering confidence in the estimated fault candidate. For the sake of brevity, the detailed explanation of the correlation estimator is not presented here and can be found in [8,10,20], where different aspects of its applicability were discussed. It is worth mentioning here that a new method based on time reversal, known as the FasTR algorithm, has been proposed recently to infer the fault location while employing the optimisation algorithm, which is time-efficient as well [6]. However, it relies on the measured/recorded transients of two terminal observation probes. In the existing EMTR methods, usually, the low-impedance fault scenarios are considered. In recent times, the EMTR-III method has been proposed to accurately locate high-impedance faults [21], and another EMTR-based method, which does not require knowledge of the fault impedance, has been reported [22]. However, these methods rely on the recorded transients of multiple observation points. The correlation estimator, on the other hand, relies on a single observation point.

Nevertheless, in the correlation estimator method, the data preparation analysis of the fault estimation stage is of utmost importance. Some characteristics require further investigation, such as (1) the necessity of fault impedance analysis, because the fault impedance might take on any value during the fault occurrence stage; therefore, an accurate guess of the fault impedance during the fault estimation stage is crucial. (2) Only the transfer functions of the three-phase fault scenario are stored in the existing correlation estimator approach. In this manner, errors in the fault location and the fault type have been observed. (3) The spatial step considered in the fault estimation stage is an additional key aspect that requires investigation. It has been observed that, if a larger spatial step is selected, there will be an error in the fault location. The correlation estimator method identifies this inaccuracy based on its CCv, but the traditional EMTR method does not.

In order to improve the correlation estimator method and make it more adaptive while tackling the aforementioned issues, three different approaches are proposed in this study. Firstly, the impact of fault impedance mismatch between the fault occurrence and fault estimation stages was analysed. It was observed that the accuracy of the method was not affected by fault locations close to the observation probes, but when the fault position moved farther away, the error in the fault estimation increased significantly. Then, a simple approach was used to address this problem by storing the transfer functions for both the low- and high-fault-impedance scenarios during the fault estimation stage. Secondly, a so-called pseudo approach was used to accurately identify the fault type and locate the fault position, in which, in the fault estimation stage, the transfer functions are stored, taking into account all possible fault types, rather than just the three-phase fault type scenario. Finally, the efficiency of the correlation estimator increased with a feasible smaller spatial step, but at the expense of higher memory space requirements for the storage devices. This is especially the case for long transmission lines that have measuring devices with larger bandwidths. This memory problem was solved by proposing a regression-analysis-based hybrid approach, in which few fault estimation stage transfer functions were selected, instead of all the data. A relationship was learned/regressed between the CCvs and their corresponding locations along the line length, ultimately predicting the actual fault position.

The structure of the paper is as follows: Section 2 discusses the basics of EMTR and the correlation estimator method. In Section 3, the impact of fault impedance mismatch is analysed. Section 4 presents a pseudo approach for the accurate identification of the fault type. The issue of the spatial step with the details is discussed in Section 5, and the regression-analysis-based hybrid approach is presented in Section 6. Finally, Section 7 concludes this paper and proposes future works.

2. EMTR and Correlation Estimator Methods

2.1. EMTR-Based Fault Location Method in Transmission Lines

To understand the application of EMTR to diagnose the fault location in transmission lines, Figure 1 is taken as a reference, where Z_T and Z_C represent the equivalent terminal impedance and the characteristic impedance of the line, respectively, while $V_f(t)$ is the fault voltage of the source, which can be a step-like function [7], or the exponential charge [8], and the fault impedance was assumed to be zero. This method can be summed up in three steps as follows [7]:

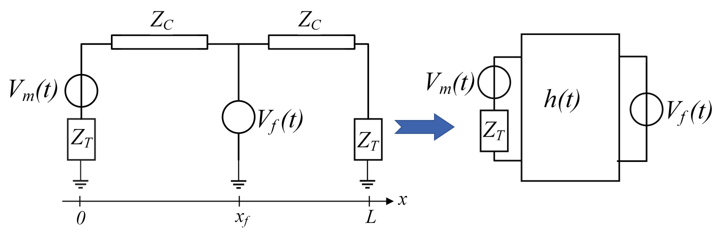

Figure 1. Simplified representation of post-fault line.

(I) Forward propagation stage: In this stage, fault-generated transient signals are measured at one of the line extremities, such as $V_m(t)$ at x = 0 in Figure 1. (II) Back-propagation stage: The measured transients in Step 1 are time-reversed and back-injected into the simulated system model from the same observation point, e.g., $V_m(T - t)$. Then, on each pre-defined GFL (x_g), the fault signals are observed. (III) Finally, the fault location is computed by employing different proposed metrics.

The recorded transients in the first step along with the necessary details are expressed in the frequency domain as follows:

$$\begin{aligned} V_m(\omega) &= \frac{(1+\rho)e^{-\gamma x_f}}{1+\rho e^{-2\gamma x_f}} V_f \\ \rho &= \frac{Z_T - Z_C}{Z_T + Z_C} \\ \gamma &= \sqrt{Z' Y'} \\ Z_C &= \sqrt{\frac{Z'}{Y'}} \end{aligned} \tag{1}$$

where x_f, ρ, γ, Z', and Y' are the fault location, reflection coefficient, propagation constant, total per-unit length impedance, and per-unit admittance, respectively. Impedance and admittance are defined as follows:

$$\begin{aligned} Z' &= j\omega L' + Z'_w + Z'_g \\ Y' &= \frac{(G' + j\omega C')Y'_g}{G' + j\omega C' + Y'_g} \end{aligned} \tag{2}$$

where $Z_w{}'$, L', C', G', $Z_g{}'$, and $Y_g{}'$ are the wire impedance, inductance, capacitance, conductance, ground impedance, and ground admittance, respectively, further defined as:

$$\begin{aligned} Z'_w &= \frac{1}{2\pi r_w}\sqrt{\left(\frac{j\omega\mu_w}{2\sigma_w}\right)} \\ L' &= \frac{\mu_0}{2\pi}\ln\left(\frac{2h}{r_w}\right) \\ C' &= \frac{2\pi\varepsilon_0}{\ln\left(\frac{2h}{r_w}\right)} \\ G' &= \frac{\sigma_{air}}{\varepsilon_0}C' \\ Z'_g &= \frac{j\omega\mu_o}{2\pi}\ln\left(\frac{1+\gamma_g h}{\gamma_g h}\right) \\ Y'_g &= \frac{\gamma_g{}^2}{Z'_g} \\ \gamma_g &= \sqrt{j\omega\mu_0(\sigma_g + j\omega\varepsilon_0\varepsilon_{rg})} \end{aligned} \tag{3}$$

where h, r_w are the height and radius of the conductor, σ_{air}, σ_g, and σ_w are the conductivity constants of the air, ground, and wire respectively, while μ_0, ϵ_0, and γ_g are the permeability, permittivity, and propagation constant in ground respectively. It is worth noticing that the line parameter expressions defined above, namely (2) and (3), are based on the line configuration with its equivalent circuit shown in Figure 2. The following is a mathematical representation of Step 2, in which the conjugated recorded transients, i.e., $V_m{}^*$, are sent back to the system [7,15]:

$$\begin{aligned} V_m{}^* &= conj(V_m) \\ V(x_g,\omega) &= \frac{(1+\rho)e^{-\gamma x_g}}{1+\rho e^{-2\gamma x_g}} V_m{}^* \\ V(x_g,\omega) &= \frac{(1+\rho)^2 e^{-\gamma\left(x_g - x_f\right)}}{\left(1+\rho e^{-2\gamma x_g}\right)\left(1+\rho e^{+2\gamma x_f}\right)} V_f{}^* \end{aligned} \tag{4}$$

Finally, in Step 3, the fault location is computed using either the energy norm or the peak amplitude norm, which are denoted as [18]:

$$x_f = \arg\Big|_{x_g} \max\left\{\left\{\int_0^T V^2(x_g,t)\,dt\right\}^{1/2}\right\} \tag{5a}$$

$$x_f = \arg\Big|_{x_g} \max\left\{\sup\left|V(x_g,t)\right|\Big|_0^T\right\} \tag{5b}$$

It is worth mentioning that the voltage signals in (5) are the time domain representation over the time period T, and these quantities are the inverse Fourier transform of the ones in (4).

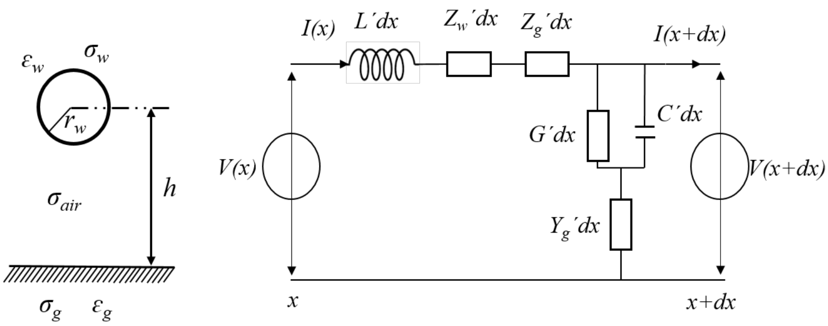

Figure 2. Single-conductor transmission line cross-section with equivalent circuit.

2.2. Correlation-Estimator-Based Fault Location Method

The correlation estimator method provides a quantitative, rather than a qualitative, interpretation. In addition, it is more of an active approach than the conventional EMTR, which can be characterised as reactive. Because there is no need to inject the time-reversed signals into the system and perform the large batches of simulations if we already have a database of the same system prior to the fault occurrence, this method is more computationally efficient. Mathematically, it can be written as follows:

$$\begin{aligned} \rho_{HH}(x_g) &= \frac{\langle H_{fos}(f) H_{fes}(f;x_g) \rangle}{\sigma_{fos}\sigma_{fes}(x_g)} \\ {\sigma_{fos}}^2 &= \left\langle \left| H_{fos}(f) \right|^2 \right\rangle \\ {\sigma_{fes}}^2 &= \left\langle \left| H_{fes}(f;x_g) \right|^2 \right\rangle \end{aligned} \tag{6}$$

As depicted in Figure 1, when the fault occurs at some point along the line, H_{fos} is the system's single output/input response, known as the fault occurrence stage transfer function. In fact, $V_m(t)$ is composed of $V_f(t)$ convoluted with $H_{fos}(t)$ in the time domain, where $V_f(t)$ is modelled here as an exponential step function, which reads [8]:

$$V_f(t) = V_0(1 - \exp(-t/T_r)) \tag{7}$$

T_r and V_0 are the rise time and peak voltage, respectively. The expression of $V_m(t)$ due to a fault can be represented in the frequency domain mathematically as

$$V_m(t) = \int_{BW} V_f(f) H_{fos}(f) e^{j2\pi f t} df \tag{8}$$

$V_f(f)$ is the fault voltage source generator in the frequency domain over the bandwidth BW, which can be defined as

$$V_f(f) = V_0 \frac{2\pi f_c}{j2\pi f(j2\pi f + 2\pi f_c)}, \quad f_c = \frac{1}{2\pi T_r} \tag{9}$$

The analytical expression of H_{fos} for a single without the branch transmission line case can be obtained from the general solution of the voltage and current expressions, which was presented in detail in [23]. Hence, the H_{fos} in its mathematical form can be written as

$$H_{fos}(f) = \frac{e^{-\gamma(x-L)} - \rho_0 e^{-\gamma(x+L)}}{(2Z_C(1-\rho_0\rho_L e^{-2\gamma L}))} \left[-\left(e^{\gamma(L-x_f)} - \rho_L e^{-\gamma(L-x_f)} \right) \right] \tag{10}$$

ρ_0 and ρ_L are the reflection coefficients at x = 0 and x = L. H_{fes} is the database of transfer functions computed at regular intervals along the line length. They can also be represented analytically as (10). σ_{fos} and σ_{fes} are the energy terms of the fault occurrence and fault estimation stage transfer functions, respectively. $\rho_{HH}(x_g)$ is the so-called correlation function, which provides the CCv corresponding to each GFL (x_g). The numerator in Equation (6) is the projection between the transfer functions of the fault occurrence and fault estimation stages, giving the measure of similarity, while the denominator provides the measure of intensity.

Since the only information available is the fault-generated transient signal (V_m), to estimate the transfer function, the assumptions of V_f proposed in [8] are considered. H_{fes}, on the other hand, are already obtained by utilising the Baum–Liu–Tesche (BLT) formulation [24,25], which was developed in the MATLAB environment. To employ the BLT formulation, Figure 3 is taken as a reference, where JF is the fault junction, while JI and J2 represent the terminal junctions. During the fault phenomena, the line is divided into two sections, shown as tubes P and Q. The problem depicted in Figure 3 is represented mathematically as follows:

$$[V] = \tfrac{1}{2}([S] + [T])([1] - [S][\Gamma])^{-1}\left[W^{(S)}\right] \tag{11}$$

$$[I] = \tfrac{1}{2}[Y_C]([S] - [T])([1] - [S][\Gamma])^{-1}\left[W^{(S)}\right] \tag{12}$$

$$\left[W^{(S)}\right] = [W_{S1}\ W_{S2}\ W_{S3}\ W_{S4}] \tag{13}$$

$$[\Gamma] = diag\left[e^{-\gamma x_f}\ e^{-\gamma x_f}\ e^{-\gamma\left(L-x_f\right)}\ e^{-\gamma\left(L-x_f\right)}\right] \tag{14}$$

$$[S] = \begin{bmatrix} 0 & S_1 & 0 & 0 \\ S_{F11} & 0 & 0 & S_{F12} \\ S_{F21} & 0 & 0 & S_{F22} \\ 0 & 0 & S_2 & 0 \end{bmatrix}; [T] = \begin{bmatrix} 0 & 1 & 0 & 0 \\ 1 & 0 & 0 & 1 \\ 1 & 0 & 0 & 1 \\ 0 & 0 & 1 & 0 \end{bmatrix} \tag{15}$$

$$[Y_C] = \left[{Z_C}^{-1}\right];\ [1] = diag[1\ \ 1\ \ 1\ \ 1] \tag{16}$$

where $W^{(S)}$ and Γ are the source super-vector and propagation super-matrix, respectively, while S, T, and Y_C are the scattering super-, identity super-, and admittance super-matrices, respectively. Finally, the transfer functions can be easily obtained from the voltage/current responses, denoted by (11) and (12).

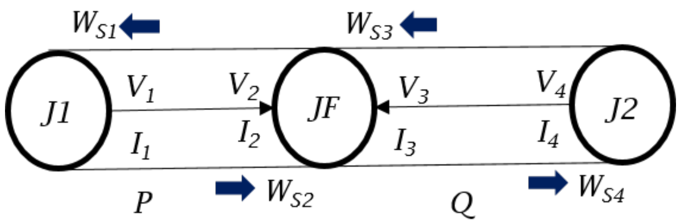

Figure 3. Fault emulation by the BLT formulation.

Now, with Figure 1 as a reference, a test fault location of 8 km on a line length of 10 km is considered by employing EMTP-RV [26,27]. Figure 4 shows the transients recorded at x = 0 due to fault voltage source $V_f(t)$ (described by Equation (7), with T_r = 10 µs, V_o = 2 kV). The time step and the time window used to record the transients are 1 µs and 7 ms, respectively. The related information of the studied analysis is given in Table 1.

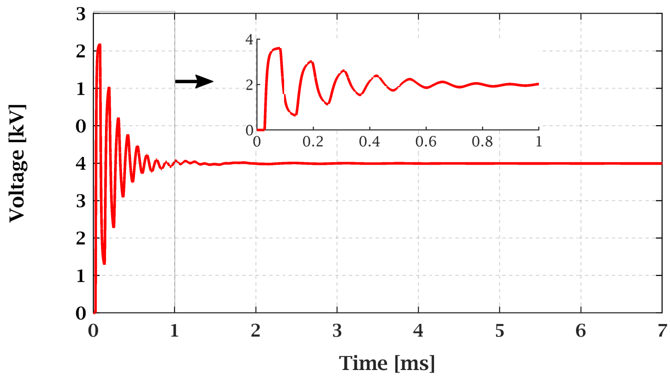

Figure 4. Fault-generated transients recorded at x = 0 due to a fault at x_f = 8 km.

Table 1. Transmission line parameters.

Parameter	Value
Height above the ground	15 m
Line length	10 km/50 km
Wire diameter	18 mm
Wire conductivity	3.7×10^{7} S/m
Air conductivity	5×10^{-15} S/m
Dielectric constant of air	8.8419×10^{-12}
Air permeability	1.2566×10^{-6}
Relative ground permittivity	10
Ground resistivity (conductivity)	100 Ωm
Load impedance's	10 kΩ

Following the steps of the EMTR conventional metric (energy metric), presented in Section 2.1, the fault location is estimated and shown in Figure 5, whereas, for the correlation estimator metric, in order to obtain the transfer function from the recorded transients, first of all, the surge compression technique is applied to these transients. It is necessary to mention that, for the accurate estimation of the transfer function, surge compression is essential. Because the discrete sampling will inevitably produce a sampling bias, this will produce additionallocation error. The surge compression technique is adopted to erase this sampling bias in the first step. Then, the inverse filter is used to filter out the fault transient signal in order to increase the location's spatial resolution; more details can be found in [20]. The corresponding result is presented in Figure 6. Then, the FFT is applied to the fault source voltage and to the surge-compressed transients (V_{m-comp}) to finally obtain the fault occurrence stage transfer function (H_{fos}), defined as

$$H_{fos} = \frac{V_{m-comp}(f)}{V_f(f)} \tag{17}$$

The fault location is then estimated using the correlation of H_{fos} and H_{fes}, which is also shown in Figure 5. The frequency spectrum from DC to 1 MHz with a step of 10 Hz is adopted during the back-propagation phase of the EMTR energy metric and the computation of H_{fes}.

The correlation estimator metric is computationally more efficient than the EMTR energy metric, as shown in Table 2, where it can be seen that, for the correlation estimator metric, the only time spent is during the pre-fault processing, whereas, during post-fault processing, it only takes a fraction of asecond to estimate the fault location. All the simulations presented in this paper were performed on an HP laptop with an Intel Core i7-4600U CPU running @ 2.10 GHz with 16 GB of RAM.

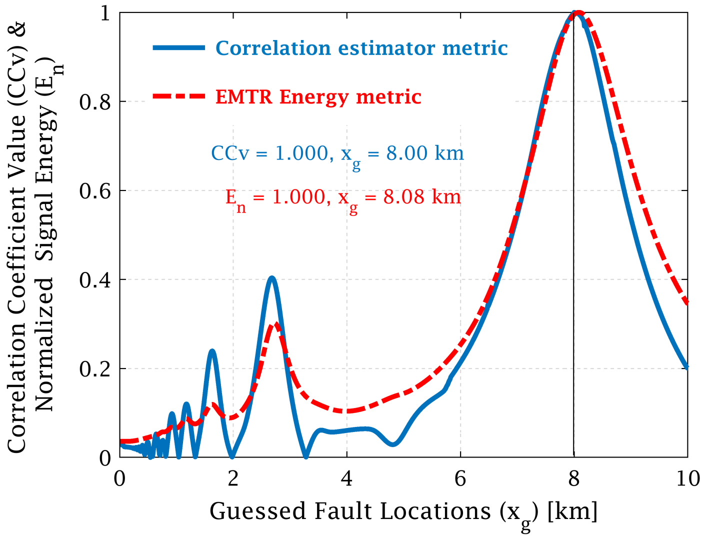

Figure 5. Correlation coefficient value and normalised signal energy as a function of GFL (x_g). The test fault location is 8 km.

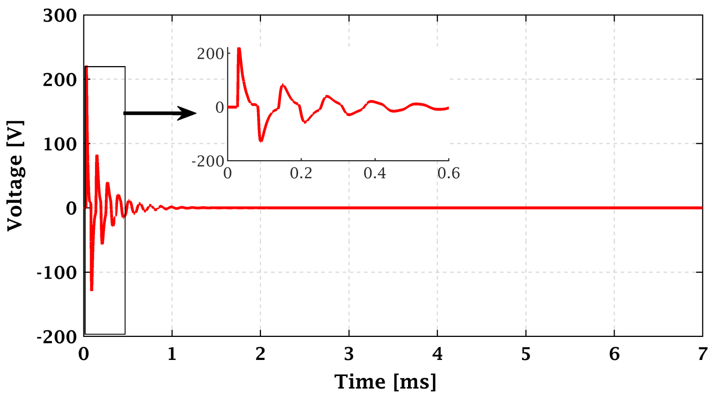

Figure 6. Surge compression by inverse filtering of the transient signal presented in Figure 4.

Table 2. Computational efficiency of the EMTR energy metric and correlation estimator metric, while considering a spatial step = 10 m and a frequency bandwidth of 100 kHz.

Line Length	EMTR Energy Metric	Correlation Estimator Metric	
	Post-Fault Processing Time	Pre-Fault Processing Time	Post-Fault Processing Time
10 km	2 min	30.96 min	2.4 s
50 km	18.3 min	2.8 h	11.59 s

In addition to being time-efficient, the correlation estimator outperforms conventional EMTR energy metric, as shown in Figure 5. This is because, when using the EMTR energy metric, there is an error in the fault location, and for the lossy case, this error increases as the fault moves away from the observation point. More importantly, when using the EMTR energy metric, it is hard to distinguish between falsely and truly estimated fault location candidates, because it uses the normalised to the maximum value criterion for the fault locations, whereas, in the correlation estimator method, the CCv corresponding to the guessed fault locations verifies the true candidate for the fault position. Therefore, the presented analysis in this paper is focused on the correlation estimator method. As the lossy transmission line case is considered throughout the entire study, the frequency-dependent line model is employed, whose accuracy is very robust and whose simulation findings were consistent with the field test results [28].

3. Impact of Fault Impedance Mismatch

As mentioned earlier, during a fault event, the fault impedance can take any value, and the accurate guess of fault impedance in the fault estimation stage is a very difficult task. In this section, the impact of the fault impedance mismatch between the fault occurrence and fault estimation stages of the correlation estimator method is presented. It is worth mentioning that the results shown in Figure 5 were obtained assuming Z_f = 10 Ω in both stages. In order to observe the impact of fault the impedance mismatch, Figure 1 and Table 1 (with line length = 50 km) are taken as references for the demonstration. The transfer functions for the fault estimation stage were obtained and stored considering Z_f = 10 Ω, whereas, in the fault occurrence stage, four different values were considered, i.e., Z_f = 0.0 Ω, 10 Ω, 300 Ω, and 1000 Ω.

For the fault estimation stage, the BLT formulation was utilised, and H_{fes} were obtained. The fault phenomenon was emulated in the EMTP-RV environment, and H_{fos} were computed for test fault locations of 8 km and 45 km. The results are shown in Figures 7 and 8 for the respective scenarios. It was observed that the fault impedance mismatch did not affect the method's accuracy for the fault locations near the observation point. As it is clear from Figure 7, when x_f = 8 km, even with a high-impedance fault, i.e., Z_f = 1000 Ω (solid black line), the GFL (x_g) was 7.98 km. The mismatch due to Z_f = 300 Ω (solid grey line) had a negligible impact as well, having GFL (x_g) = 7.99 km. The respective CCvs, i.e., 0.7941 and 0.8861, confirmed the mismatch between the fault occurrence and fault estimation stages. When the values of Z_f in both stages were equal or almost similar, only then GFL (x_g) = x_f.

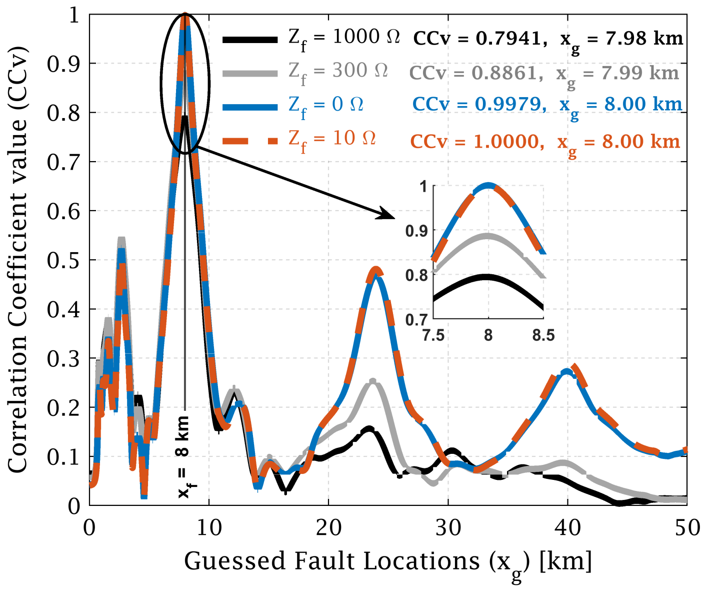

Figure 7. CCvs as a function of the GFL (x_g): considering different values of Z_f in the fault occurrence stage, while in the fault estimation stage, Z_f = 10 Ω; the test fault location is 8 km.

On the other hand, as the fault position moved away, the location error became significant in the presence of a mismatch. As can be seen in Figure 8, for x_f = 45 km considering Z_f = 1000 Ω (solid black line) and 300 Ω (solid grey line) in the fault occurrence stage, the GFL (x_g) was 44.71 km and 44.84 km, respectively. This impact can be eliminated by employing a simple approach, i.e., separately storing H_{fes} for low and high impedance faults. In other words, whenever a fault occurs, its related H_{fos} would be correlated with each H_{fes} of a low- and high-impedance fault, respectively. Then, the best candidate for the GFL (x_g) would be selected based on the higher CCv. This becomes clear by looking at

Figure 9, where the results presented in Figure 8 were obtained considering Z_f = 1000 Ω in the fault estimation stage. It can be seen that the fault location was estimated accurately, which was also confirmed by CCv = 1.00. In addition, H_{fos} due to Z_f = 300 Ω was correlated with a low and high fault impedance H_{fes}, and two GFLs (x_g) were computed, i.e., 44.84 km and 45.07 km, respectively. The best candidate among these two will be decided based on the corresponding CCv, and in this case, the CCv of 45.07 km was 0.9501, which is higher than 0.8603 (solid grey line).

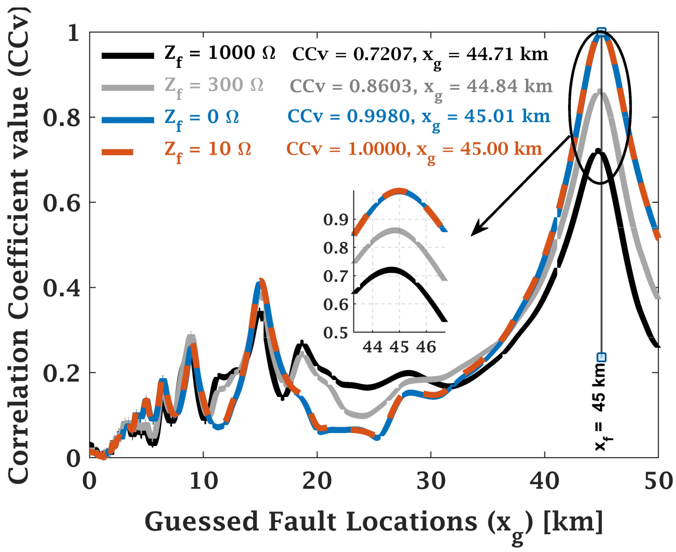

Figure 8. CCvs as a function of the GFL (x_g): considering different values of Z_f in the fault occurrence stage, while in the fault estimation stage, Z_f = 10 Ω; the test fault location is 45 km.

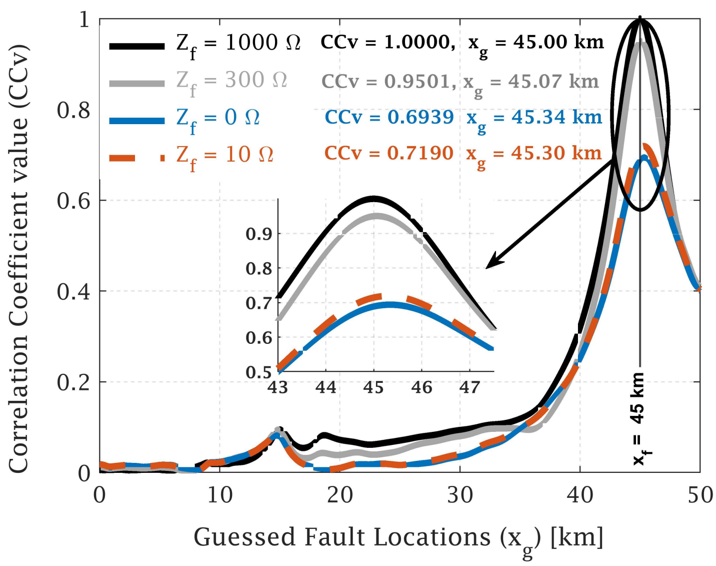

Figure 9. CCvs as a function of the GFL (x_g): considering different values of Z_f in the fault occurrence stage, while in the fault estimation stage, Z_f = 1000 Ω; the test fault location is 45 km.

A comprehensive analysis of the impact of the fault impedance mismatch along the line length was performed, which is shown in Figures 10 and 11. It can be seen that, in all cases, the impact was almost negligible for fault locations up to 25 km, and the impact is presented in the form of the relative location error, defined as

$$e[\%] = \frac{|x_f - x_g|}{L} \times 100 \quad (18)$$

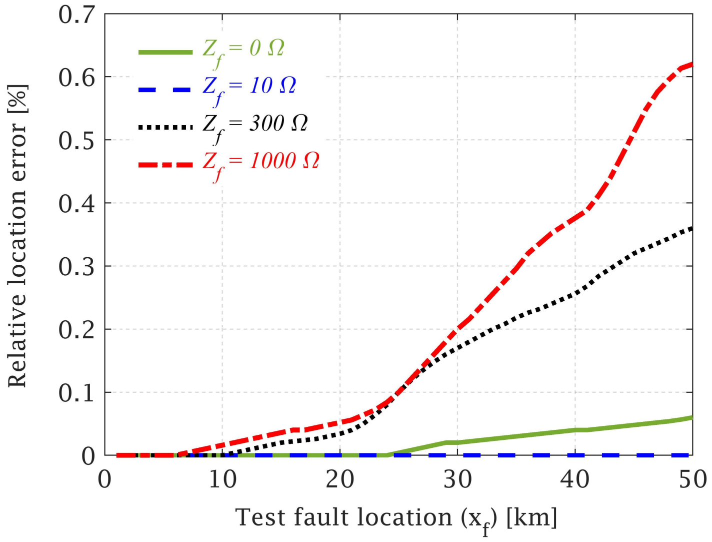

Figure 10. Impact of the fault impedance mismatch along the line length in terms of the relative location error; in the fault occurrence stage, four different values of fault impedance are considered, while in the fault estimation stage, Z_f = 10 Ω.

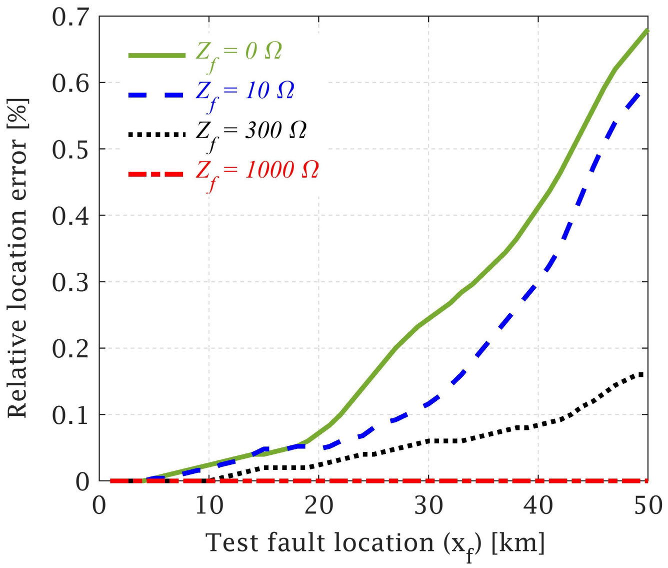

Figure 11. Impact of the fault impedance mismatch along the line length in terms of the relative location error; in the fault occurrence stage, four different values of fault impedance are considered, while in the fault estimation stage, Z_f = 1000 Ω.

On the other hand, as the fault location moves away from the observation point, the impact increased for the cases of Z_f = 300 Ω and Z_f = 1000 Ω, while, in the fault estimation stage, Z_f = 10 Ω, as shown in Figure 10.

A similar pattern was observed for the cases of Z_f = 0 Ω and Z_f = 10 Ω, when Z_f = 1000 Ω was assumed in the fault estimation stage, as shown in Figure 11. Therefore, this analysis shows that both low and high fault impedances should be taken into account during the fault estimation stage to obtain more accurate results. Then, the fault location candidate with the highest CCv should be selected.

4. Identification of Fault Type with Accuracy

The issue of fault type identification for a three-phase transmission line is discussed in this section. In this regard, a 345 kV frequency-dependent transmission line system with the configuration illustrated in Figure 12 was investigated; other related parameters were already presented in Table 1. The corresponding total p.u.l. transmission line impedance and admittance matrices at f = 1 kHz are as follows:

$$\mathbf{Z}' = \begin{bmatrix} 0.96 + 13.1i & 0.86 + 4.5i & 0.86 + 3.6i \\ 0.86 + 4.5i & 0.96 + 13.16i & 0.86 + 4.5i \\ 0.86 + 3.6i & 0.86 + 4.5i & 0.96 + 13.16i \end{bmatrix} \Omega/\text{km}$$
$$\mathbf{Y}' = \begin{bmatrix} 5.5e^{-5}{+}43i & 4.9e^{-5}{-}7.6i & 4.7e^{-5}{-}3.6i \\ 3.8e^{-5}{-}7.6i & 4.3e^{-5}{+}44i & 3.8e^{-5}{-}7.6i \\ 4.7e^{-5}{-}3.6i & 4.9e^{-5}{-}7.6i & 5.5e^{-5}{+}43i \end{bmatrix} \mu\text{S/km} \quad (19)$$

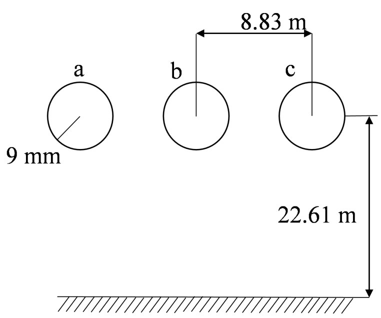

Figure 12. Cross-section representation of three-phase transmission line.

The fault phenomenon was simulated in an EMTP-RV environment, shown in Figure 13, and H_{fos} was obtained for each phase (explained in Section 2.2), whereas, H_{fes} were computed at regular spatial steps along the line by solving the multi-conductor transmission line equation using the BLT formulation (also presented in Section 2).

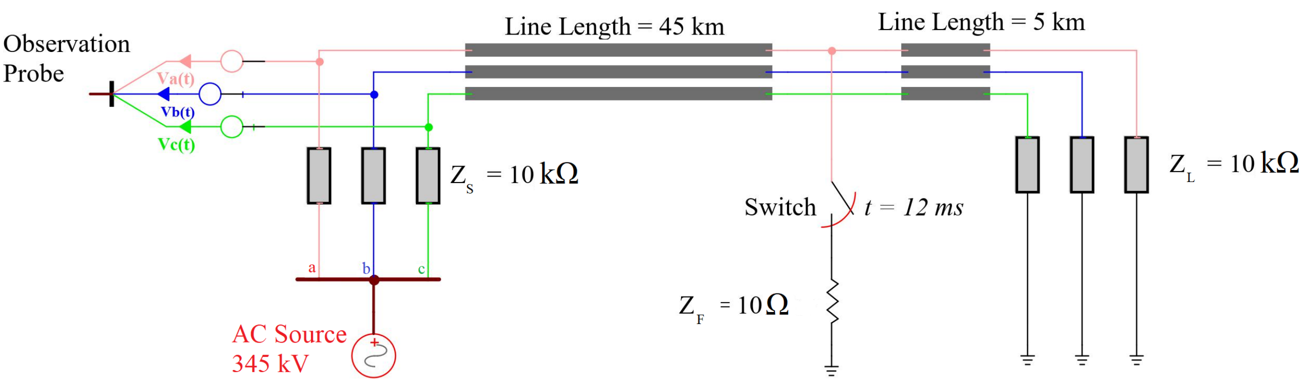

Figure 13. Schematic representation of the system under study, implemented in EMTP–RV.

For any fault type scenario, three H_{fes} must be stored in principle. It was observed that, if only the H_{fes} of a three-phase fault scenario were correlated with H_{fos}, then the accuracy of the method would be affected. For instance, a fault location of 45 km in Phase "a" was considered, and the related H_{fos} were correlated with the H_{fes} of the three-phase fault scenario, as shown in Figure 14. The GFL(x_g) were inconsistent over all three phases, with values of 43.9 km, 46.9 km, and 47.30 km for Phases a, b, and c, respectively. Despite the fact that the CCv of Phase "a" was greater, i.e., 0.8416, identifying the faulty phase, the estimated fault location was inaccurate. A similar pattern was observed in other scenarios, which are presented comprehensively in Table 3. This was because of the coupling phenomena that exist between the phases. The data in Table 3 are written as (CCv, x_g (km)).

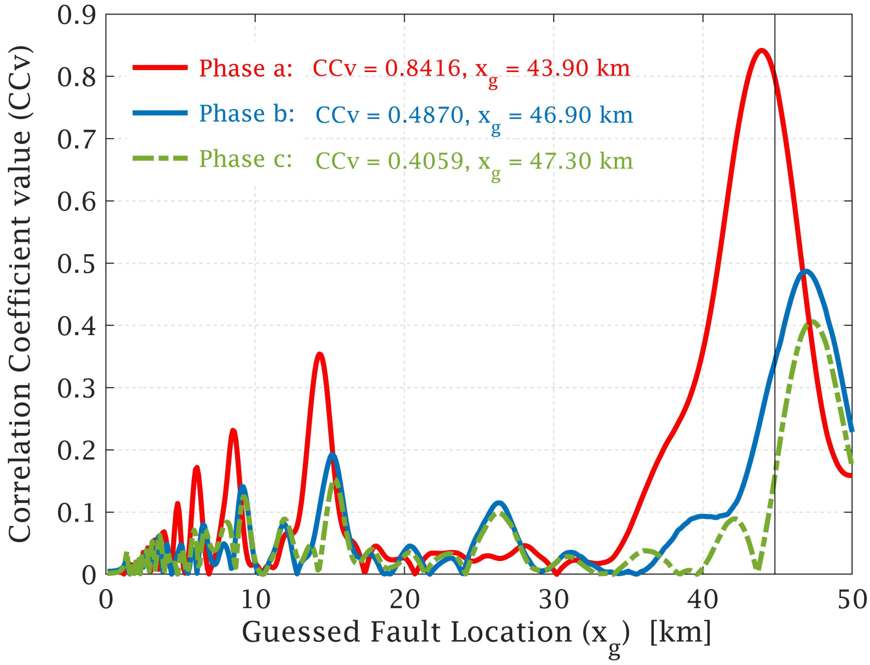

Figure 14. CCvs as a function of the GFL (x_g): a fault is considered in Phase "a" at 45 km and estimated in all three phases, while the correlation of the H_{fos} and H_{fes} of the 3-phase fault type scenario is shown.

Table 3. Test fault location of 45 km having different fault types scenarios and its estimation (CCv, x_g) in each phase by the pseudo approach.

Fault Type	Estimation	Simulation Storage Data		
		Phase a	**Phases ab**	**Phases abc**
Phase a	a	**1.00, 45.0**	0.902, 44.6	**0.841, 43.9**
	b	**1.00, 45.0**	0.474, 47.0	**0.487, 46.9**
	c	**1.00, 45.0**	0.713, 45.0	**0.405, 47.3**
Phases ab	a	0.898, 45.8	**1.00, 45.0**	0.941, 44.7
	b	0.506, 41.7	**1.00, 45.0**	0.919, 44.7
	c	0.713, 45.0	**1.00, 45.0**	0.425, 46.8
Phases abc	a	0.864,46.4	0.945, 45.8	**1.00, 45.0**
	b	0.534, 43.1	0.926, 45.9	**1.00, 45.0**
	c	0.459, 42.5	0.495, 43.3	**1.00, 45.0**

In order to address this issue, another so-called pseudo approach is proposed, in which the H_{fes} for all the possible fault types, e.g., Phases a, b, c, ab, bc, ca, and abc, were stored. For the sake of simplicity, only three scenarios are written in Table 3. Whenever the fault event will occur, to identify the fault type, H_{fos} will be correlated with all the storage data one by one. This will be decided based on the CCv and the consistency of the GFL (x_g) in all three phases.

For demonstration purposes, the identical fault scenario in Phase "a" at 45 km was repeated, but this time, the related H_{fos} were correlated with H_{fes} of the Phase "a" fault type. Figure 15 illustrates that the CCvs in all three phases were "1.00" and that the GFL (x_g) were equally consistent and accurate, i.e., 45 km. Thus, the storage data of the fault estimation stage, at which the so-called "symmetry condition" is satisfied, determine both the fault type and the location.

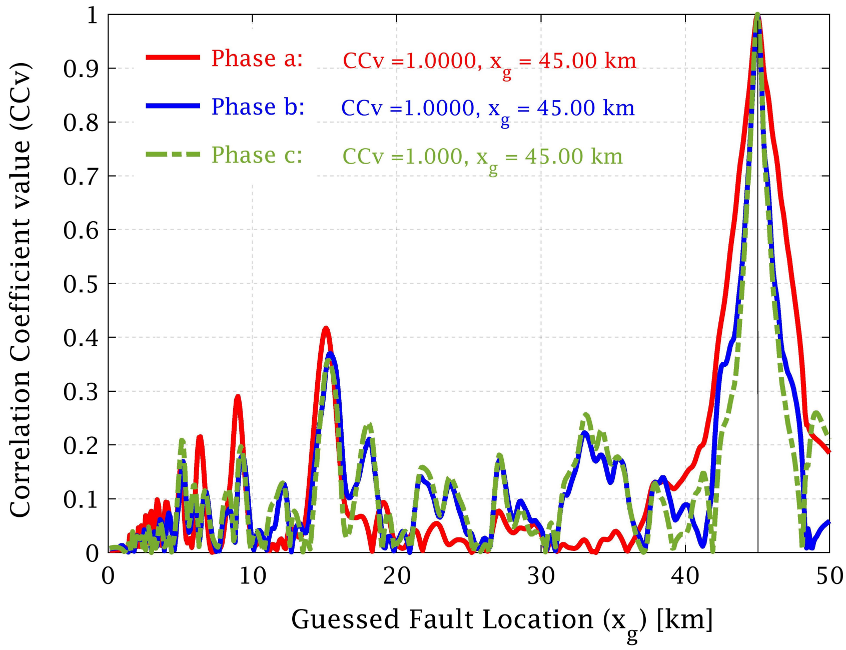

Figure 15. CCvs as a function of the GFL (x_g): the fault is considered In Phase "a" at 45 km and estimated in all three phases, while the correlation between the H_{fos} and H_{fes} of the Phase "a" fault type scenario is given.

5. Influence of Spatial Step in EMTR Methods

5.1. Issue of Spatial Step in the Fault Estimation Stage

During the fault estimation stage of the EMTR-based fault location methods, the significance of the spatial step (Δg) cannot be overlooked. Firstly, a comparison is presented between the EMTR energy metric and the correlation estimator method while assessing this issue. For both techniques, a simulation considering a certain spatial step was performed; in the EMTR energy metric, the simulation was run after the fault occurrence, and in the correlation estimator, it was already completed before the fault event, which is why it is a time-efficient approach and, hence, preferred.

For illustration purposes, x_f = 8.25 km along the line length of 10 km was considered. The results are shown in Figures 16 and 17 for the EMTR energy metric and the correlation estimator method, respectively. Four different values of the spatial steps were selected in the fault estimation stage, e.g., Δg = 1000 m (solid blue line), 500 m (dashed purple line), 100 m (dotted-dashed red line), and 10 m (dotted black line). From the figures, it can be seen that, with a larger spatial step, there was location error in the GFL (x_g), and as the spatial step became smaller, the fault detection accuracy increased.

Moreover, once again, the advantage of the correlation estimator metric was confirmed by the results shown in Figure 17, where CCv = 1.0000 as the deciding criterionfor the accurate guess of the test fault location, i.e., $x_f = x_g$. Unlike the EMTR energy metric, as shown in Figure 16, there is no clear and distinctive definition to decide between the true and false estimations. As it uses a global normalisation, i.e., En = 1 (normalised to the maximum value) as the fault location criterion, so all the GFLs (x_g) could be the best candidates for the true fault location.

5.2. Memory Burden on Data Storage Devices

The results reported in the previous subsection show that the correlation estimator has a few advantages over the EMTR energy metric. However, in order to improve the fault detection accuracy further, the fault estimation stage should use the smallest spatial step possible. As highlighted in Table 4, it is quite clear that this was only possible when Δg = 10 m; only then, the fault position was estimated accurately. However, this would increase the volume of data (number of H_{fes} along the line length), which is an extra burden for data storage devices. Moreover, this data volume would increase further for long transmission line lengths and high-frequency bandwidths, as highlighted in Table 5.

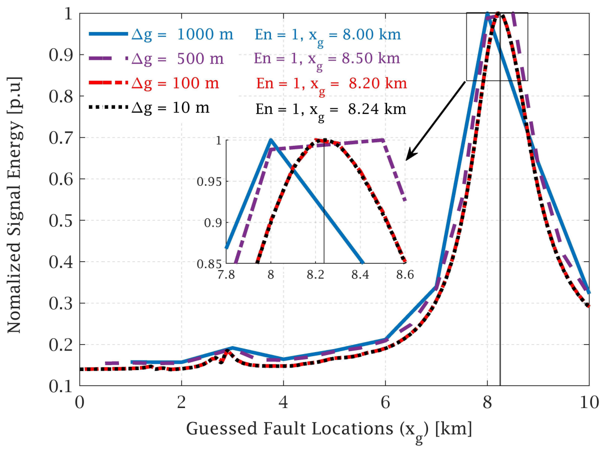

Figure 16. EMTR energy metric: considering different spatial steps in the fault estimation stage. The test fault location is 8.25 km.

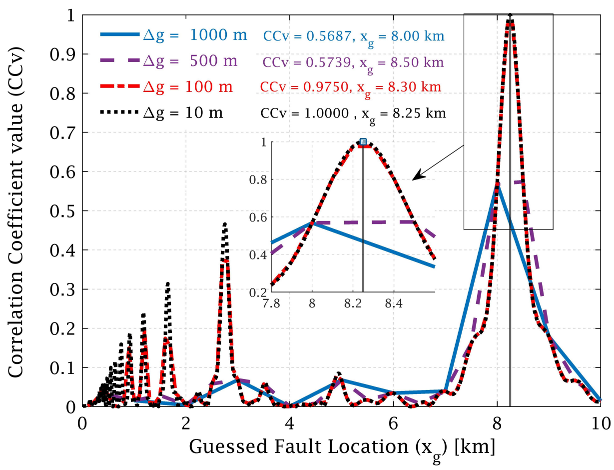

Figure 17. Correlation estimator: considering different spatial steps in the fault estimation stage. The test fault location is 8.25 km.

Table 4. Correlation estimator: fault location accuracy for different spatial steps in the fault estimation stage.

Test Fault Locations (x_f) (m)	Simulated Phase Spatial Step			
	1000 m	**500 m**	**100 m**	**10 m**
	Guessed Fault Location (x_g) (m)			
20	1000	500	100	**20**
370	1000	500	400	**370**
2750	3000	2500	2800	**2750**
7320	7000	7500	7300	**7320**
18,690	19,000	19,000	18,800	**18,690**
23,980	24,000	24,000	24,100	**23,980**
34,110	34,000	34,500	34,300	**34,110**
42,540	43,000	43,000	42,800	**42,540**
46,070	46,000	46,500	46,400	**46,070**
48,880	49,000	49,000	49,200	**48,880**

Table 5. Existing correlation estimator: memory space required for different spatial steps in the fault estimation stage.

Transmission Line Length	Frequency	Simulated Phase Spatial Step			
		1000 m	**500 m**	**100 m**	**10 m**
		Memory Space Required			
50 km	DC-1 MHz	73 MB	146 MB	733 MB	**7.40 GB**
	DC-5 MHz	370 MB	741 MB	3.67 GB	**35.25 GB**
100 km	DC-1MHz	147 MB	295 MB	1.47 GB	**14.9 GB**
	DC-5 MHz	748 MB	1.5 GB	7.35 GB	**74.5 GB**

It is clear that gigabytes (GB) of storage space are required to obtain accurate results. To address this issue and further improve the correlation estimator method, this work proposes a hybrid approach, which combines a correlation estimator with regression analysis.

6. Regression-Analysis-Based Hybrid Approach

Figure 1 is considered again, and the relevant information was already presented in Table 1. In this approach, first, H_{fes} with a smaller Δg were obtained and correlated with the transfer functions at fewer selected positions, obtaining the CCvs at those locations. The relationship between the CCvs and line lengths (with a smaller possible Δg) was learned to construct a regression model. This model was then used for fault location prediction on new CCvs (obtained by correlating the selected transfer functions with the fault occurrence stage transfer function). Therefore, fewer H_{fes} needed to be stored instead of all of the H_{fes} and, in this way, ultimately relieving the memory burden of the data storage devices.

The MATLAB regression learner app (RLA) was used for the regression analysis [29]. In this application, the training data were imported and trained with the available regression models. Based on their statistical properties, the best-fit models were selected, which were then evaluated on new data and and exported for future use as standalone applications. The available regression models in RLA are linear regression, decision trees, Gaussian process regression, support vector machines, and ensembles of tree.

Five locations were selected along the line length of 50 km as the storage locations, e.g., x_g (SL) = [10 m, 12,500 m, 25,000 m, 37,500 m, 49,990 m]. The transfer functions corresponding to these positions are known as storage transfer functions (H_{STF}). These H_{STF} were then correlated with H_{fes} (obtained at Δg = 10 m), and the CCvs were computed utilising Equation (6), mathematically written as follows:

$$CCvs(x_g[SL]) = \frac{\langle H_{STF}(f;x_g[SL])H_{fes}(f;x_g[\Delta g{=}10\text{ m}])\rangle}{\sigma(x_g[SL])\sigma(x_g[\Delta g{=}10\text{ m}])} \tag{20}$$

These CCvs served as the independent variable, and a line length of 50 km with a spatial step of Δg = 10 m was taken as the dependent variable. This training dataset was imported into MATLAB RLA to learn the relationship, employing all the available models. Table 6 displays the statistical outcomes of these models. It is important to note that, for the sake of simplicity, only models with substantial outputs are listed in the table, where MSE = mean-squared error, RMSE = root-mean-squared error, MAE = mean absolute error, and R^2 = determination coefficient, which are mathematically defined as [30]

$$\begin{aligned} MSE &= \frac{\sum_{i=1}^{N}(y_i-\hat{y}_i)^2}{N-(q+1)}\ ;\ RMSE = \sqrt{MSE} \\ MAE &= \frac{100}{N}\sum_{i=1}^{N}\left|\frac{y_i-\hat{y}_i}{y_i}\right|\ ;\ R^2 = 1-\frac{\sum_{i=1}^{N}(y_i-\hat{y}_i)^2}{\sum_{i=1}^{N}(y_i-\bar{y})^2} \end{aligned} \tag{21}$$

$\bar{y}$, y_i, and $\hat{y}_i$ are the mean, observed, and fit values of the dependent variable, respectively, whereas N and q are the total No. of observations and predictors, respectively. On the basis of these parameter values, the performance of the regression models was evaluated and the best-fit model was selected.

Table 6. Statistical outputs of regression models.

Regression Model	RMSE	R^2	MAE	Training Time (s)
Tree Fine	159	1	108	5.49
Tree Medium	170	1	112	3.2
SVM Fine Gaussian	1787	0.98	1654	69.75
SVM Medium Gaussian	1292	0.99	1147	14.8
Ensemble Bagged Trees	178	1	49	24.6
GPR Squared Exponential	72	1	18	837.26
GPR Matern 5/2	27	1	8	1218
GPR Exponential	**18**	**1**	**5.11**	**1991**
GPR Rational Quadratic	35	1	12	2450

As can be seen in Table 6, the Gaussian process regression (GPR) models outperformed the other regression models. In addition, GPR exponential has the lowest RMSE value = 18 and a determination coefficient value (R2) of "1". Although the other regression models also had a determination coefficient value of "1", the RMSE is considered the best criterion for the decision; moreover, the model that gave the required results would be the best choice [30]. The response plot at one of the storage locations for GPR exponential is shown in Figure 18. It is clear that there was a perfect agreement between the regression estimation and the training sample data. After training the data, the regression models were tested on new data, which were obtained by correlating H_{STF} with H_{fos} of some random fault locations along the line (e.g., 20 m, 370 m, 2750 m, 7320 m, 18,690 m, 23,980 m, 34,110 m, and 42,540 m), mathematically defined as

$$CCvs(new) = \frac{\langle H_{fos}(f)H_{STF}(f;x_g[SL])\rangle}{\sigma_{fos}\sigma_{STF}(x_g[SL])} \quad (22)$$

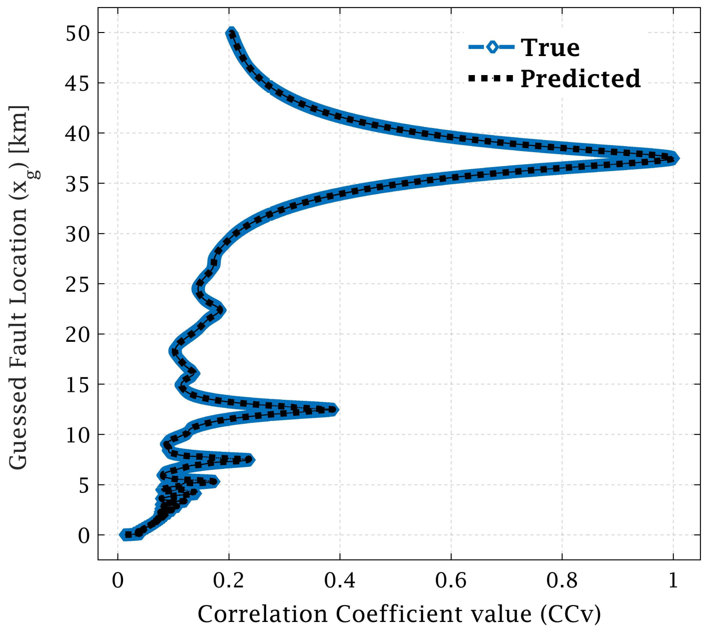

Figure 18. Response plot of GPR exponential at one of the storage locations, i.e., 37,500 m.

It was observed that the GPR models provided more precise and consistent fault location estimation. As shown in Figure 19, the exponential model produced more promising outcomes within the GPRs, with the error near zero. The absolute error is mathematically denoted as

$$Absolute\ Error\ (m) = \left| x_f - x_g \right| \tag{23}$$

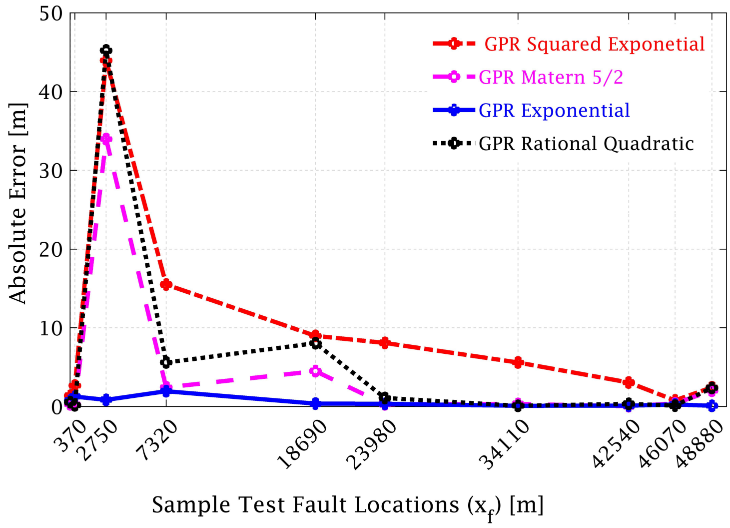

Figure 19. Comparison of the GPR models in the prediction of fault locations.

As the objective of this presented analysis was to reduce the amount of memory space required, the case was made to show that a fault can be computed accurately with just a few transfer functions and a regression model. Table 7 compares the memory requirements of the hybrid technique and the existing correlation estimator (with a smaller spatial step). It is obvious that only tens or hundreds of megabytes were required, as opposed to allotting gigabytes (GBs) of memory for H_{fes}. For instance, for the case of line length = 100 km and frequency spectrum = DC-5MHz, while employing the existing correlation estimator, the memory space requirement was 75 GB, whereas, the same job could be performed with 80 MB by taking advantage of the machine learning algorithms.

Table 7. Memory space requirement: comparison between the existing correlation estimator and the hybrid approach.

Transmission Line Length	Frequency	Memory Space Required	
		Existing Correlation	Hybrid Approach
50 km	DC-1 MHz	7.40 GB	**7.9 MB**
	DC-5 MHz	35.25 GB	**38.9 MB**
100 km	DC-1 MHz	14.9 GB	**15.9 MB**
	DC-5 MHz	74.5 GB	**79.7 MB**

As discussed in Section 3, two separate copies of H_{fes} are required for low- (Z_f = 10 Ω) and high-impedance (Z_f = 1000 Ω) fault scenarios to locate the fault position accurately. This will, however, use more memory space; therefore, a hybrid approach can be applied to both scenarios independently to alleviate the large memory requirement for the data storage devices. Consequently, the fault location processes can be stated as follows: whenever a fault occurs, H_{fos} will be correlated with H_{STF} of low- and high-impedance faults. The regression model and H_{STF} for fault location prediction will be selected based on the maximum CCv of the two scenarios. For instance, in Figure 20, it can be seen that the H_{fos} due to x_f = 10 km with Z_f = 0 Ω was correlated with H_{STF} of low- and high-impedance faults, and the CCv of H_{STF} @ Z_f = 10 Ω was higher. Therefore, for fault prediction, this scenario was selected to give 10.05 km. Similarly, for H_{fos} due to x_f = 35 km with Z_f = 500 Ω, as the CCv of H_{STF} @ Z_f = 1000 Ω was higher, so it would be utilised for fault prediction, which was 35.13 km.

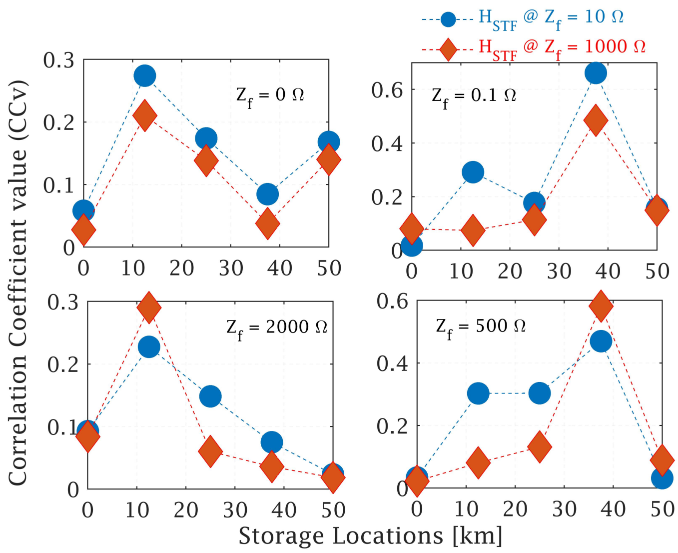

Figure 20. Correlation of low- and high-impedance fault—H_{STF} with H_{fos} due to x_f = 10 km with Z_f = 0 Ω and 2000 Ω (**left column**) and with H_{fos} due to x_f = 35 km with Z_f = 0.1 Ω and 500 Ω (**right column**).

The pseudo approach described in Section 4 will also require additional memory, because it takes GBs to store just one copy of H_{fes}; as we mentioned in the case of a single-conductor transmission line, so the more memory space will be needed to store transfer function copies for each fault type. The memory burden once again was reduced by employing the hybrid approach, as argued before. The results provided in Table 3 are repeated in Table 8 using the hybrid method (requiring only a few selected transfer functions with a regression model). Even with a few selected transfer functions, the similarity of the results in Tables 3 and 8 is evident. It is important to note that, although a new database must be generated when the system topology is altered, this will not influence the method's efficiency because the data are prepared prior to fault occurrences, and this is not repeated.

Table 8. Test fault location of 45 km having different scenarios of fault types and its estimation by the pseudo and hybrid approaches.

Fault Type	**Estimation ($x_g{'}$)**	**Fault Estimation Stage Storage Data**		
		Phase a	**Phases ab**	**Phases abc**
Phase a	a	**44.99**	40.73	36.2
	b	**45**	29.09	32.4
	c	**44.99**	37.2	28.5
Phases ab	a	39.8	**45.05**	46.9
	b	49.5	**45**	43.8
	c	43.5	**44.99**	29.4
Phases abc	a	38.35	46.63	**45**
	b	38.8	35.71	**44.9**
	c	30.66	27.25	**45**

7. Conclusions

In this paper, some key issues relating to the fault estimation stage of the correlation estimator method were analysed. First of all, the impact of the fault impedance mismatch between the fault occurrence and fault estimation stages was discussed. An error in the fault location was observed for the fault positions far from the observation point. To tackle this problem, a simple approach was proposed in which the fault estimation stage transfer functions are stored separately for low- and high-impedance faults. Secondly, a new pseudo method was developed to correctly identify fault types and pinpoint their precise locations, in which the fault estimation stage transfer functions were stored for all possible fault types.

Finally, the important issue of the spatial step, considered in the fault estimation stage of conventional EMTR and the correlation estimator methods, was studied. Meanwhile, the advantage of the latter method was also highlighted, which was based on the CCv. It was shown that only a smaller spatial step ensures the fault location's accuracy, but at the cost of more memory space required. This problem was solved by proposing a hybrid approach utilising a mixture of the correlation estimator method and regression analysis, in which a few locations along the line length were selected to store their corresponding transfer functions. These transfer functions were correlated with the transfer functions having a smaller spatial step to provide the CCv. The line length and CCv then served as the training data for the regression model's construction, and the Gaussian process regression was the best-fit model to predict the fault location. It was demonstrated that, by employing the existing correlation estimator, the memory space requirement was 75 GB, whereas the same job could be performed with 80 MB by taking advantage of the proposed approach.

The hybrid approach was also applied in conjunction with the simple and pseudo approaches. It is important to note that the current analyses were based on theoretical and simple cases. Complex networks will be investigated in future studies, and the experimental validation of the method proposed will be presented using field data from real-world systems. Moreover, the study of nonlinear fault impedance scenarios with uncertain parameters is already in progress.

Author Contributions: Conceptualization, A.N.; Methodology, A.N.; Software, A.N. and S.H.; Validation, Y.X. and S.H.; Formal analysis, S.H.; Investigation, Y.X.; Resources, Y.X.; Writing—original draft, A.N.; Writing—review & editing, S.H., N.D., P.C. and M.S.; Supervision, Y.X.; Project administration, Y.X.; Funding acquisition, Y.X. All authors have read and agreed to the published version of the manuscript.

Funding: This research was funded by the National Natural Science Foundation of China under Grant 52007139.

Conflicts of Interest: The authors declare no conflict of interest.

References

1. Saha, M.M.; Izykowski, J.; Rosolowski, E. *Fault Location on Power Networks*; Springer: Berlin/Heidelberg, Germany, 2010; Volume 2.
2. Dashti, R.; Salehizadeh, S.M.; Shaker, H.R.; Tahavori, M. Fault Location in Double Circuit Medium Power Distribution Networks Using an Impedance-Based Method. *Appl. Sci.* **2018**, *7*, 1034. [CrossRef]
3. Wang, S.; Xu, G. Research on travelling wave fault technology based on ground potential. *AIP Adv.* **2021**, *11*, 115009. [CrossRef]
4. Lopes, F.V.; Lima, P.; Ribeiro, J.P.G.; Honorato, T.R.; Silva, K.M.; Leite, E.J.S.; Neves, W.L.A.; Roch, G. Practical methodology for two-terminal travelling wave-based fault location eliminating the need for line parameters and time synchronization. *IEEE Trans. Power Deliv.* **2019**, *34*, 2123–2134. [CrossRef]
5. Furse, C.M.; Kafal, M.; Razzaghi, R.; Shin, Y.-J. Fault diagnosis for electrical systems and power networks: A review. *IEEE Sens. J.* **2020**, *21*, 888–906. [CrossRef]
6. Kafal, M.; Gregis, N.; Benoit, J.; Ravot, N. An effective method based on time reversal and optimization techniques for locating faults on power grids. *IEEE Sens. J.* **2020**, *21*, 1092–1099. [CrossRef]
7. Razzaghi, R.; Lugrin, G.; Manesh, H.; Romero, C.; Paolone, M.; Rachidi, F. An efficient method based on the electromagnetic time reversal to locate faults in power networks. *IEEE Trans. Power Deliv.* **2013**, *28*, 1663–1673. [CrossRef]
8. He, S.; Cozza, A.; Xie, Y. Electromagnetic time reversal as a correlation estimator: Improved metrics and design criteria for fault location in power grids. *IEEE Trans. Electromagn. Compat.* **2019**, *62*, 598–611. [CrossRef]

9. He, S.; Cozza, A.; Xie, Y. On the spatial resolution of fault-location techniques based on full-fault transients. *IEEE Trans. Power Deliv.* **2019**, *35*, 1527–1540. [CrossRef]
10. Cozza, A.; He, S.; Xie, Y. Impact of propagation losses on fault location accuracy in full transient-based methods. *IEEE Trans. Power Deliv.* **2020**, *36*, 383–396. [CrossRef]
11. Rachidi, F.; Rubinstein, M.; Paolone, M. *Electromagnetic Time Reversal: Application to EMC and Power Systems*; John Wiley & Sons: Hoboken, NJ, USA, 2017.
12. Wang, T.; Qiu, S.; Shi, L.-H.; Li, Y. Broadband VHF localization of lightning radiation sources by EMTR. *IEEE Trans. Electromagn. Compat.* **2017**, *59*, 1949–1957. [CrossRef]
13. Razzaghi, R.; Lugrin, G.; Paolone, M.; Rachidi, F. On the use of electromagnetic time reversal to locate faults in series-compensated transmission lines. In Proceedings of the IEEE Grenoble Conference, Grenoble, France, 16–20 June 2013; pp. 1–5.
14. Razzaghi, R.; Paolone, M.; Rachidi, F.; Descloux, J.; Raison, B.; Retière, N.; Retière, N. Fault location in multi-terminal HVDC networks based on electromagnetic time reversal with limited time reversal window. In Proceedings of the Power Systems Computation Conference, Wroclaw, Poland, 18–22 August 2014; pp. 1–7.
15. Codino, A.; Wang, Z.; Razzaghi, R.; Paolone, M.; Rachid, F. An alternative method for locating faults in transmission line networks based on time reversal. *IEEE Trans. Electromagn. Compat.* **2017**, *59*, 1601–1612. [CrossRef]
16. Wang, Z.; Razzaghi, R.; Paolone, M.; Rachidi, F. Electromagnetic time reversal applied to fault location: On the properties of back-injected signals. In Proceedings of the Power Systems Computation Conference, Dublin, Ireland, 11–15 June 2018; pp. 1–7.
17. Wang, Z.; Codino, A.; Razzaghi, R.; Paolone, M.; Rachidi, F. Using electromagnetic time reversal to locate faults in transmission lines: Definition and application of the "Mirrored Minimum Energy" property. In Proceedings of the International Symposium on Electromagnetic Compatibility-EMC EUROPE, Angers, France, 4–8 September 2017; pp. 1–6.
18. He, S.; Xie, Y.; Wang, Z.-Y.; Rachidi, F.; Liu, B.; Li, Q.; Kong, X. Norm criteria in the electromagnetic time reversal technique for fault location in transmission lines. *IEEE Trans. Electromagn. Compat.* **2018**, *60*, 1240–1248. [CrossRef]
19. Wang, Z.; He, S.; Li, Q.; Liu, B.; Razzaghi, R.; Paolone, M.; Xie, Y.; Rubin-stein, M.; Rachidi, F. A full-scale experimental validation of electromagnetic time reversal applied to locate disturbances in overhead power distribution lines. *IEEE Trans. Electromagn. Compat.* **2018**, *60*, 1562-1570. [CrossRef]
20. Cozza, A.; He, S.; Xie, Y. Surge compression for improved fault location accuracy in full transient-based methods. *IEEE Sens. J.* **2020**, *21*, 995–1008. [CrossRef]
21. An, J.; Zhuang, C.; Rachidi, F.; Zeng, R. An effective EMTR-based high-impedance fault location method for transmission lines. *IEEE Trans. Electromagn. Compat.* **2020**, *63*, 268–276. [CrossRef]
22. Sun, J.; Yang, Q.; Cui, H.; Ran, J.; Liu, H. Distribution line fault location with unknown fault impedance based on electromagnetic time reversal. *IEEE Trans. Electromagn. Compat.* **2021**, *63*, 1921–1929. [CrossRef]
23. Tesche, F.M.; Ianoz, M.; Karlsson, T. *EMC Analysis Methods and Computational Models*; John Wiley & Sons: Hoboken, NJ, USA, 1996.
24. Baum, C.E.; Liu, T.K.; Tesche, F.M. On the analysis of general multiconductor transmission-line networks. *Interact. Note* **1978**, *350*, 467–547.
25. Parmantier, J.; Alliot, J.; Labaune, G.; Degauque, P. Electromagnetic topology: Junction characterization methods. *Interact. Note* **1990**, *489*, 1–12.
26. Dommel, H.W. Digital computer solution of electromagnetic transients in single-and multiphase networks. *IEEE Trans. Power Appar. Syst.* **1969**, *4*, 388–399. [CrossRef]
27. Mahseredjian, J.; Dennetire, S.; Dubé, L.; Khodabakhchian, B.; Gérin-Lajoie, L. On a new approach for the simulation of transients in power systems. *Electr. Power Syst. Res.* **2007**, *77*, 1514–1520. [CrossRef]
28. Marti, J.R. Accurate modelling of frequency-dependent transmission lines in electromagnetic transient simulations. *IEEE Trans. Power Appar. Syst.* **1982**, *101*, 147–157. [CrossRef]
29. Ekici, S.; Unal, F.; Ozleyen, U. Comparison of different regression models to estimate fault location on hybrid power systems. *IET Gener. Transm. Distrib.* **2019**, *13*, 4756–4765. [CrossRef]
30. Ostertagová, E. Modelling using polynomial regression. *Procedia Eng.* **2012**, *48*, 500–506. [CrossRef]